# Slope efficiency and spurious-free dynamic range of silicon Mach-Zehnder modulator upon carrier depletion and injection effects

Xianshu Luo,[1,*] Xiaoguang Tu,[1] Junfeng Song,[1,3] Lu Ding,[2] Qing Fang,[1] Tsung-Yang Liow,[1] Mingbin Yu,[1] and Guo-Qiang Lo[1]

[1]*Institute of Microelectronics, A\*STAR (Agency for Science, Technology and Research), 11 Science Park Road, Science Park II, 117685 Singapore*
[2]*Institute of Materials Research and Engineering, A\*STAR (Agency for Science, Technology and Research), 117602 Singapore*
[3]*State Key Laboratory on Integrated Opto-Electronics, College of Electronic Science and Engineering, Jilin University, Changchun, 130012 People's Republic of China*
*\*luox@ime.a-star.edu.sg*

**Abstract:** We investigate the performances of a silicon PN-junction Mach-Zehnder modulator for analog application. The slope efficiency and spurious-free dynamic range (SFDR) of such a modulator upon carrier depletion and carrier injection effects are characterized and compared. Input RF frequency-dependence measurements show that the depletion-type modulator is usually with ~20 dB·Hz$^{2/3}$ higher SFDR comparing to the injection-type modulator, yet with an order-of-magnitude lower slope efficiency. For the depletion-type and injection-type modulators, the measured maximum SFDRs are respectively ~95 dB·Hz$^{2/3}$ and 75 dB·Hz$^{2/3}$, with maximum slope efficiency of 0.3 V$^{-1}$ and 8 V$^{-1}$. We numerically model the SFDR by using the experimentally extracted effective refractive index change, which shows good agreement with the measurements.

©2013 Optical Society of America

OCIS codes: (040.6040) Silicon; (230.2090) Electro-optical devices; (130.0130) Integrated optics; (230.4110) Modulators.

## References and links

1. J. Capmany and D. Novak, "Microwave photonics combines two worlds," Nat. Photonics **1**(6), 319–330 (2007).
2. C. H. Cox, *Analog Optical Links: Theory and Practice* (Cambridge Univ. Press, 2004).
3. C. H. Cox III, E. I. Ackerman, G. E. Betts, and J. L. Prince, "Limits on the performance of RF-over-fiber links and their impact on device design," IEEE Trans. Microw. Theory Tech. **54**(2), 906–920 (2006).
4. R. Soref, "The past, present and future of silicon photonics," IEEE J. Sel. Top. Quantum Electron. **12**(6), 1678–1687 (2006).
5. B. Jalali and S. Fathpour, "Silicon photonics," J. Lightwave Technol. **24**(12), 4600–4615 (2006).
6. R. A. Soref and B. R. Bennet, "Electrooptical effects in silicon," IEEE J. Quantum Electron. **23**(1), 123–129 (1987).
7. G. T. Reed, G. Mashanovich, F. Y. Gardes, and D. J. Thomson, "Silicon optical modulators," Nat. Photonics **4**(8), 518–526 (2010).
8. W. M. Green, M. J. Rooks, L. Sekaric, and Y. A. Vlasov, "Ultra-compact, low RF power, 10 Gb/s silicon Mach-Zehnder modulator," Opt. Express **15**(25), 17106–17113 (2007).
9. L. Liao, A. Liu, D. Rubin, J. Basak, Y. Chetrit, H. Nguyen, R. Cohen, N. Izhaky, and M. Paniccia, "40Gbit/s silicon optical modulator for high-speed applications," Electron. Lett. **43**(22), 1196–1197 (2007).
10. N.-N. Feng, S. Liao, D. Feng, P. Dong, D. Zheng, H. Liang, R. Shafiiha, G. Li, J. E. Cunningham, A. V. Krishnamoorthy, and M. Asghari, "High speed carrier-depletion modulators with 14V-cm V_πL integrated on 025µm silicon-on-insulator waveguides," Opt. Express **18**(8), 7994 (2010).
11. N.-N. Feng, S. Liao, D. Feng, D. P. Dong, D. Zheng, H. Liang, R. Shafiiha, G. Li, J. E. Cunningham, A. V. Krishnamoorthy, and M. Asghari, "High speed carrier-depletion modulators with 1.4V-cm V$_π$L integrated on 0.25µm silicon-on-insulator waveguides," Opt. Express **18**, 7994–7999 (2010).
12. X. Tu, T.-Y. Liow, J. Song, M. Yu, and G. Q. Lo, "Fabrication of low loss and high speed silicon optical modulator using doping compensation method," Opt. Express **19**(19), 18029–18035 (2011).
13. M. Ziebell, D. Marris-Morini, G. Rasigade, J.-M. Fédéli, P. Crozat, E. Cassan, D. Bouville, and L. Vivien, "40 Gbit/s low-loss silicon optical modulator based on a pipin diode," Opt. Express **20**(10), 10591–10596 (2012).

14. P. Dong, L. Chen, and Y.-K. Chen, "High-speed low-voltage single-drive push-pull silicon Mach-Zehnder modulators," Opt. Express **20**(6), 6163–6169 (2012).
15. F. Vacondio, M. Mirshafiei, J. Basak, Ansheng Liu, Ling Liao, M. Paniccia, and L. A. Rusch, "A silicon modulator enabling RF over fiber for 802.11 OFDM signals," IEEE J. Sel. Top. Quantum Electron. **16**(1), 141–148 (2010).
16. X. Luo, X. Tu, J. Song, T. Y. Liow, Q. Fang, P. H. Lim, Y. Xiong, M. Yu, and G. Q. Lo, "Characterization of silicon electro-optical modulators for microwave photonic links," in Proc. 2011 IEEE MWP, 109–112 (2011).
17. A. Ayazi, T. Baehr-Jones, Y. Liu, A. E.-J. Lim, and M. Hochberg, "Linearity of silicon ring modulators for analog optical links," Opt. Express **20**(12), 13115–13122 (2012).
18. M. Song, L. Zhang, R. G. Beausoleil, and A. E. Willner, "Nonlinear distortion in a silicon microring-based electro-optical modulator for analog optical links," IEEE J. Sel. Top. Quantum Electron. **16**(1), 185–191 (2010).
19. A. Karim and J. Devenport, "Noise figure reduction in externally modulated analog fiber-optic links," IEEE Photon. Technol. Lett. **19**(5), 312–314 (2007).
20. B. Liu, J. Shim, Y. Chiu, A. Keating, J. Piprek, and J. Bowers, "Analog characterization of low-voltage MQW traveling-wave electroabsorption modulators," J. Lightwave Technol. **21**(12), 3011–3019 (2003).

## 1. Introduction

RF-/Microwave-photonics [1] has gained widespread applications to analog optical links such as radio-over-fiber, phase-arrayed antenna, antenna remoting for radar systems, subcarrier transmission, etc. As one of the key building blocks in microwave photonic links, optical modulator plays an important role for the E/O conversion. In order to determine the performance of an optical modulator for the E/O conversion, several performance metrics are considered, including the modulation efficiency, the RF gain, and the nonlinearity [2,3]. While the modulation efficiency can be determined by measuring the half-wave voltage, the RF gain is characterized by measuring the slope efficiency (SE), and the nonlinearity is determined by measuring the spurious-free dynamic range (SFDR).

Meanwhile, the unprecedented growth of the silicon photonics [4,5] has driven the development of silicon-based electro-optical modulators using free-carrier dispersion effect [6]. High-speed silicon Mach-Zehnder Interferometer (MZI) modulators [7–14] either with carrier injection or carrier depletion have been demonstrated over the past few years. However, only few works engaged in the performance characterization of Si optical modulators for analog application [15–18]. Furthermore, although the depletion-type modulator [9–14] has been demonstrated to be with higher modulation speed (up to 40 Gb/s) than that of the injection-type modulator [8] (< 10 Gb/s), there is lack of the performance comparison for analog application.

In this paper, we investigate the analog performance of a PN-junction silicon MZI modulator upon carrier depletion and injection effects. We show the detailed comparison of the slope efficiency (SE) and the spurious-free dynamic range of such depletion- and injection-type modulators. The experiments show that, the injection-type modulator has much higher modulation efficiency and slope efficiency, while the depletion-type modulator usually has relatively higher SFDRs. For the depletion-type and injection-type modulators, the measured maximum SFDRs are respectively ~95 dB·Hz$^{2/3}$ and 75 dB·Hz$^{2/3}$, with maximum slope efficiency of 0.3 V$^{-1}$ and 8 V$^{-1}$. We numerically model the SFDR by using extracted effective refractive index change and show consistence to the experimental results. It also shows that the difference between the depletion-type and injection-type modulators originates from the strong nonlinear plasma dispersion effect of the free-carrier injection effect.

## 2. Theory

Spurious-free dynamic range (SFDR) is a critical parameter for modulators in analog application. It is used for the characterization of the modulator nonlinearities, which originates from the nonlinear refractive index change mainly due to the nonlinear plasma dispersion effect for MZI modulator [18]. The SFDR is defined as the difference in the RF input in the link between the signal level that produces an output equal to the noise level and the signal level that produces distortion products equal to the noise level. Due to the optical nonlinearity, in addition to the carrier, there will be second-order harmonic distortion (SHD), third-order harmonic distortion (THD), third-order inter-modulation distortion (IMD3), and other higher order nonlinear terms in the output RF signal. In the sub-octave RF link, the

performance is mainly affected by the IMD3, as the other high-order harmonic distortions are out of the band. Thus, we only focus on the investigation of the IMD3 in this work. Suppose the input RF signal includes two tones at frequencies of $f_1$ and $f_1 + \Delta f$, the output RF signal will include four frequency components $f_1, f_1 + \Delta f, f_1 - \Delta f$, and $f_1 + 2\Delta f$ in the sub-octave, which originates from the nonlinear plasma dispersion effect [6].

For a MZI modulator, the transfer function can be expressed as

$$P_{out} = \frac{P_{in}}{2}[1 + \cos(\phi_0 + \Delta\phi)] \tag{1}$$

where $\phi_0$ is the modulator bias angle from 0 to $\pi$, and $\Delta\phi$ is the phase change induced by the refractive index change, which can be calculated as

$$\Delta\phi = 2\pi \frac{\Delta n_{eff} L}{\lambda} \tag{2}$$

where $\Delta n_{eff}$ is the effective refractive index change and $L$ is the length of the MZI phase shift arm.

In practice, the effective refractive index change $\Delta n_{eff}$ of a MZI modulator can be obtained by measuring the optical phase shift upon different biased voltages, which can be expressed as

$$\Delta n_{eff} = \frac{n_g \Delta L}{L} \frac{\Delta\lambda}{\lambda} \tag{3}$$

where $\Delta L$ is the physical length difference between two MZI arms, $\lambda$ is the resonance wavelength, $\Delta\lambda$ is the resonance shift, and $n_g$ is the group index, which can be calculated via:

$$n_g = \frac{\lambda^2}{FSR \cdot \Delta L} \tag{4}$$

with $FSR$ the free-spectral range.

On the other hand, the refractive index change as a function of applied voltage can be expressed as

$$\Delta n_{eff}(t) = P_0 + P_1 V(t) + P_2 V^2(t) + P_3 V^3(t) + O(V) \tag{5}$$

where the $P_0$, $P_1$, $P_2$, $P_3$ can be extracted by polynomial fitting the obtained refractive index changes using Eqs. (3) and (4).

If two-tone method is applied to determine the SFDR, the input voltage is with the form of:

$$V(t) = V_{o1} \sin(2\pi f_1 t) + V_{o2} \sin[2\pi(f_1 + \Delta f)t] \tag{6}$$

Substituting Eqs. (5) and (6) into Eqs. (2) and (1), we can obtain the generated multiple frequency components from the output of the MZI modulator.

## 3. Device fabrication and characterization

We adopt a low-loss Si MZI modulator with ion implantation compensation [12]. The fabrication starts from a 200-mm silicon-on-insulator (SOI) wafer with 220 nm silicon thickness and 2 μm buried oxide (BOX). We first do the blanket ion implantation compensation, followed by a two-step silicon reactive ion etching (RIE) to form a rib waveguide for ion implantation and a channel waveguide for the nano-taper. The waveguide width is 0.6 μm. The length of the phase shift is 4 mm. The slab for the P$^+$ and N$^+$ Ohmic contact implantation is with thickness of ~95 nm. P and N type implantations are subsequently performed, followed with rapid thermal anneal at 1030 °C for 5 second. A ~1.2 μm oxide is deposited as an upper cladding, followed by contact holes opening. Finally,

aluminum is deposited and patterned to form the contact pads. The detailed designs and fabrication process of such MZI modulator can be referred to our previous demonstrations [10,12].

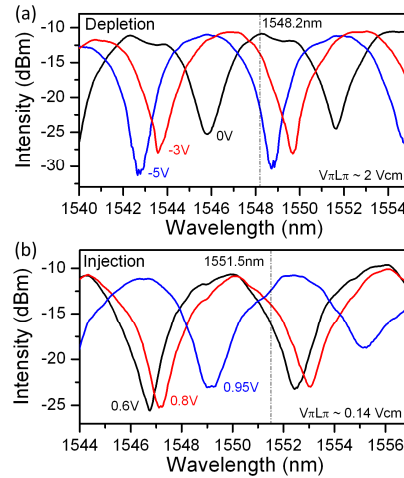## 3.1 Device characterization



Fig. 1. The normalized transmission spectra of (a) depletion-type and (b) injection-type modulator upon different DC bias voltages.

We first investigate the optical transmission responses upon different DC bias. We use a broadband amplified spontaneous emission (ASE) as the light source and an optical spectrum analyzer (OSA) to record the transmission spectra. Figures 1(a) and 1(b) show the normalized optical transmission spectra upon reverse and forward DC biases for respectively depletion- and injection-type modulation. For both cases, the modulator insertion loss is ~10 dB, including the input/output coupling loss, the Y-splitter loss, and the phase shifter loss. For the reverse-biased depletion-type modulator, the resonance wavelength blue-shifts with the biased voltage induced increment in the refractive index, while for the forward-biased injection-type modulator, the resonance wavelength red-shifts with the biased voltage induced reduction in the refractive index. We mention that the direction of the resonance wavelength shift is determined by the supplying of the voltage to different MZI arms. The resonance wavelength shift is in the opposite direction if the bias voltages are supplied to another MZI arm. The obvious difference is that the half-wave voltage $V_\pi$ is only ~0.35 V for injection-type modulator, while is ~5 V for the depletion-type modulator. This results in the significant difference of the phase shifter efficiency $V_\pi \cdot L_\pi$ of ~0.14 V·cm for the injection-type modulator, comparing to ~2 V·cm for the depletion-type modulator. This shows an order-of-magnitude enhanced phase shift efficiency by using forward-biased injection-type modulator. Considering the threshold voltage of ~0.6 V for the injection-type modulator, we calculate the $V_\pi$ starting from 0.6 V, which is within the PN diode working range.
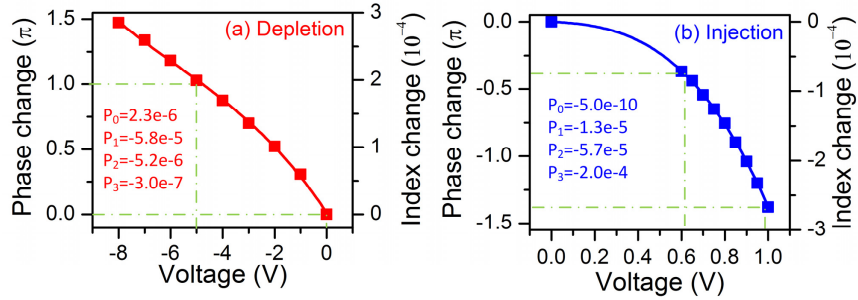
Fig. 2. The measured phase changes upon different biased voltages for (a) depletion-type modulator and (b) injection-type modulator. The calculated effective refractive index change is also illustrated with 3rd-order polynomial fitting. The lines are the polynomial fitting curves. The green dash-dotted lines indicate the half-wave voltage changes.

Based on the transmission spectra measurements, we can obtain the optical phase change using Eq. (2). Figures 2(a) and 2(b) show the measured optical phase change as functions of the biased voltages for depletion-type and injection-type modulators. The illustrations clearly show the half-wave voltages are respectively ~5 V and ~0.35 V. The calculated effective refractive index changes using Eq. (3) are also shown in Figs. 2(a) and 2(b) with third-order polynomial fitting. The results show clearly that the injection-type modulator is with high nonlinearity comparing to the depletion-type modulator, which is confirmed by the fitted nonlinear parameters. For $\pi$ phase shift, the effective refractive index change is $\sim 2 \times 10^{-4}$, which is consistent with our previous demonstration [12].
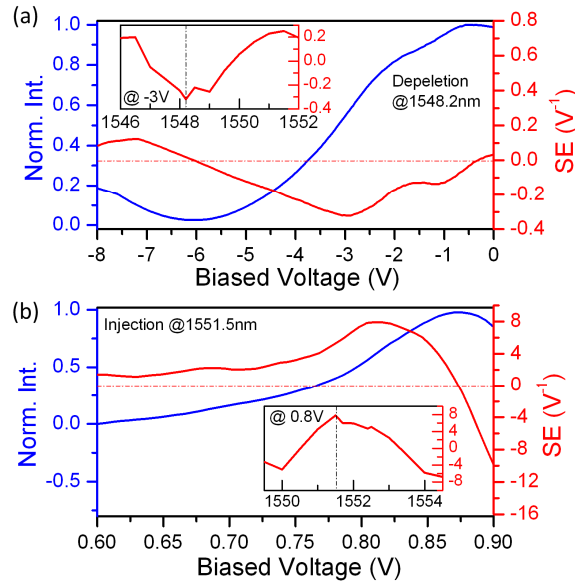


Fig. 3. Measured optical intensity and the extracted DC slope efficiency of (a) depletion-type and (b) injection-type modulator as functions of the DC bias voltages. Insert: The wavelength-dependence slope efficiency at fixed bias voltages for both (a) depletion-type and (b) injection-type modulators.

We investigate the DC slope efficiency by measuring the output power of the modulator against the DC bias voltages at fixed wavelength. The blue lines in Figs. 3(a) and 3(b) show the normalized optical intensity as function of the biased voltages respectively for depletion-type and injection-type modulators. For the depletion-type modulator, the optical intensity at 1548.2 nm decreases as the increase of the reverse biased voltage from 0V to −6 V and reach

the minimum. Whereas for the injection-type modulator, the optical intensity at 1551.5 nm increases as the increase of the forward-biased voltage till ~0.88 V. Such optical intensity variations are consistent with the transmission measurements as shown in Fig. 1.

The DC slope efficiency can be calculated from the measured intensity response. The red lines in Figs. 3(a) and 3(b) show the extracted slope efficiency. For the depletion-type modulator, the maximum slope efficiency at 1548.2 nm is only ~-0.3 $V^{-1}$. In contrast, for the injection-type modulator, the maximum slope efficiency at 1551.5 nm is as high as 8 $V^{-1}$, suggesting an order-of-magnitude higher slope efficiency. The insets in Figs. 3(a) and 3(b) show the wavelength-dependence slope efficiency at fixed bias voltages, which suggest the maximum value at the selected carrier wavelengths for both types of modulators. Hereafter, we will fix the carrier wavelengths and DC bias voltages for the SFDR measurements.

*3.2 Spurious-free dynamic range*

The SFDR can be measured by using two-tone method. Figure 4 shows the block diagram of the two-tone measurement setup. A CW laser sitting at carrier wavelength is end-firing to an erbium-doped fiber amplifier (EDFA) in order to boost up the optical power to overcome the total link loss. The light then passes through an optical tunable bandpass filter (BPF) in order to filtering out the spontaneous emission noise and a polarization controller before coupling into the silicon chip via a polarization maintaining lensed fiber. Two RF signals with frequencies at $f_1$ and $f_1 + \Delta f$ are generated using two identical signal generators and combined by a high-speed power combiner after low-pass filters. A bias tee is inserted in order to bias the input signal. The combined RF signal is supplying to one of the MZI arms by using single-arm driving scheme. The output optical signal from the silicon modulator is collected by another lensed fiber, detected by a high-speed (40 GHz) photodiode, and finally recorded by a high-speed (67 GHz) spectrum analyzer. The measured output optical power from the CW laser is ~6 dBm, and the input optical power to the silicon waveguide is ~10 dBm. Thus, considering the fiber-to-waveguide coupling loss of ~3 dB/facet, the optical power reaching to the MZI modulator is ~7 dBm. The input RF powers for the two tones can be read from the signal generator while the output RF powers for the four harmonics at $f_1$, $f_1 + \Delta f$, $f_1 - \Delta f$, and $f_1 + 2\Delta f$ are directly read out from the spectrum analyzer.
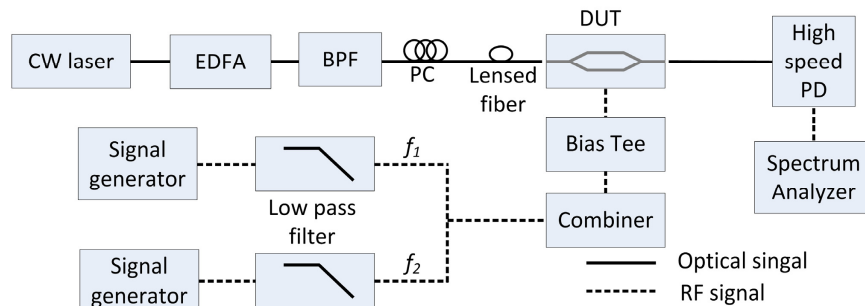


Fig. 4. Block diagram of the two-tone measurement setup. EDFA: erbium-doped fiber amplifier, BPF: bandpass filter; PC: polarization controller, DUT: device under test, PD: photodiode.

Figure 5(a) shows the measured output RF powers of the carrier and IMD3 as functions of the input RF power for the reverse-biased depletion-type modulator. The carrier wavelength is selected at 1548.2 nm with DC bias voltage of −3 V. The input RF frequency $f_1$ is 500 MHz and $\Delta f$ is 1 MHz. The frequency offset $\Delta f$ is selected large enough in order for the spectrum analyzer to resolve the adjacent frequency components. However, we confirm that the SFDR is independence on such frequency offset. For both carrier and IMD3, the output power linearly increases until saturated. The measured noise floor (NF) at 10 kHz is ~-121 dBm, corresponding to a noise floor of −161 dBm/Hz. Thus, the extracted SFDR is ~90 dB·$Hz^{2/3}$. Similarly, we also measured the SFDR of the forward-biased injection-type modulator at

carrier wavelength of 1551.5 nm with DC bias of 0.8 V, as shown in Fig. 5(b). The extracted SFDR is ~70 dB·Hz$^{2/3}$. As for comparison, we also measure a commercial lithium niobate MZI modulator using the same setup with an SFDR of ~112 dB·Hz$^{2/3}$, which is consistent with the measurement of ~120 dB·Hz$^{2/3}$ in [19]. Furthermore, the measured SFDR of an electroabsorption modulator is 128 dB·Hz$^{4/5}$ with a slope efficiency of 4 V$^{-1}$ [20], and is ~90 dB·Hz$^{2/3}$ for a silicon microring modulator [17]. The relatively low SFDR for silicon-based modulator is mainly due to the relatively strong nonlinearity of the plasma dispersion effect [6].
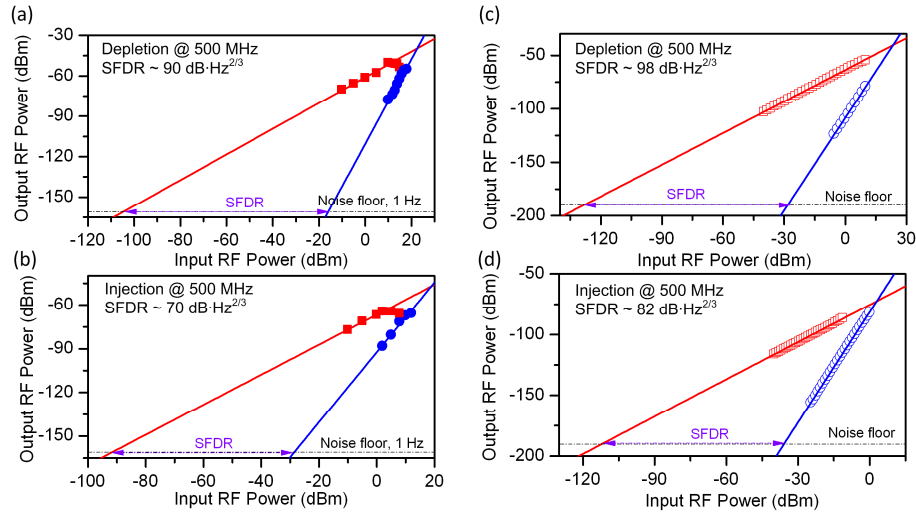


Fig. 5. (a)-(b) The measured RF output power as function of input RF power for (a) depletion-type and (b) injection-type modulators with $f_1$ = 500 MHz center frequency and $\Delta f$ = 1 MHz. (c)-(d) The modeled RF output power as function of input RF power for (c) depletion-type and (d) injection-type modulator.

We also numerically model the SFDRs of the depletion- and injection-type modulators by using the modeling described in Sec. 2 and the obtained nonlinear coefficients from the extracted effective refractive index change (Fig. 2). In the modeling, we assume an optical insertion loss of 15 dB at the operation wavelength. The photodetector responsivity is set to be 0.4 A/W and the loading impedance is assumed to be 50 Ω. The modulator bias angle $\phi_0$ is set to be $\pi/2$ for quadrature point operation. Figures 5(c)-5(d) show the modeled RF output power upon the different input RF powers for depletion-type and injection-type modulators. The calculated noise floor is ~-185 dBm. Thus, the calculated SFDR are respectively ~98 dB·Hz$^{2/3}$ and 82 dB·Hz$^{2/3}$, which are consistent with our measurements.

We measure the SFDR at different RF frequencies for both depletion- and injection-type modulators. The measured 3-dB bandwidths are respectively ~8 GHz and 1 GHz for depletion-type and injection-type modulators. Thus, we select the maximum operation frequencies of 1 GHz. The solid squares and circles in Fig. 6 summarize the measured SFDR. The measured maximum SFDR is ~95 dB·Hz$^{2/3}$ for the depletion-type modulator and ~75 dB·Hz$^{2/3}$ for the injection-type modulator. In general, the SFDR of the depletion-type modulator is ~20 dB·Hz$^{2/3}$ higher than those of the injection-type modulator. We attribute this to the large free-carrier generation for the injection-type modulator induced strong optical nonlinearity, which is shown in Fig. 2 for the effective refractive index change. The modeled SFDRs are also included for comparison, with maximum values of ~100 dB·Hz$^{2/3}$ and 83 dB·Hz$^{2/3}$ for depletion- and injection-type modulators. The experimental and modeling results agree very well.
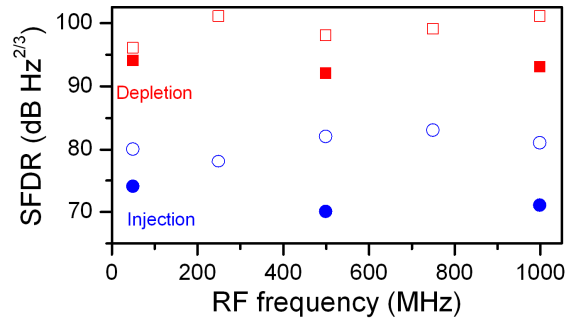
Fig. 6. The measured (solid squares and circles) and modeled (opened squares and circles) SFDRs depending on the RF frequency for both depletion-type and injection-type modulators.

## 4. Discussion and conclusion

We characterized a Si PN-diode MZI modulator under carrier-depletion and carrier-injection effects for RF photonic application. The analog performances, including slope efficiency and spurious-free dynamic range (SFDR), are measured and compared. The experiments suggest that while injection-type modulator shows an order-of-magnitude higher slope efficiency, the depletion-type modulator is usually with 20 dB·Hz$^{2/3}$ higher SFDR at different input RF frequencies. Such measurement results are verified by numerical modeling and show good agreement.

Although the demonstrated Si MZI modulator shows relatively small bandwidth upon both depletion and injection effects, it is applicable for higher speed modulation as demonstrated by other groups previously. In general, most of the depletion-type MZI modulators are with bandwidth larger than 10 GHz [9–14], while the optimized injection-type MZI modulator can operate with ~10 Gb/s data rate [8]. Thus, in view of different analog applications, it is of importance to choose different types of modulators. For the application requiring high modulation speed (> 10 Gb/s) and high SFDR, it is better to choose the depletion-type modulator. Whereas, for the application requiring moderate modulation speed (< 10 Gb/s) and high slope efficiency, the injection-type modulator is a better choice.

## Acknowledgment